



Cooperative Trajectory Tracking and Stability Control with Improved Stability Criterion for Intelligent Four-Wheel-Independent-Drive Electric Vehicles

Lei Zhang¹ · Liquan Sun² · Xiaolin Ding³ · Zhenpo Wang³

Received: 27 March 2024 / Accepted: 13 December 2024 / Published online: 24 February 2025
© China Society of Automotive Engineers (China SAE) 2025

Abstract

Accurate trajectory tracking control with guaranteed vehicle dynamics stability is fundamental for automated vehicles. This paper proposes an enabling trajectory tracking scheme with improved dynamics stability for four-wheel-independent-drive electric vehicles. First, a modified phase plane method is proposed for assessing vehicle dynamics stability by constructing a 3-D phase trajectory. Then a lateral trajectory tracking controller is developed using a model predictive control algorithm with a variable stiffness tire model. Considering the effect of the additional yaw moment on the trajectory tracking error and vehicle yaw stability, a dual-weight cooperative sliding mode control method is established for yaw angle tracking compensation and yaw stability control through target switching. Finally, the desired additional yaw moment and total longitudinal tire force are achieved through wheel torque allocation while accounting for the slip ratios. The performance of the proposed method is evaluated through comprehensive Hardware-in-the-Loop tests under double-lane change maneuvers.

Keywords Intelligent four-wheel-independent-drive electric vehicles · Trajectory tracking · Yaw stability · Cooperative control

Abbreviations

FWID EV	Four-wheel-independent-drive electric vehicle
PID	Proportional, integral, and derivative
SMC	Sliding model control
MPC	Model predictive control
DOF	Degree of freedom
CoG	Center of gravity
HIL	Hardware-in-the-Loop

1 Introduction

Automated vehicles hold the promise of significantly improving the fuel economy, safety, and traffic efficiency of the ground transportation system. Efficient emergency avoidance is necessary for ensuring driving safety especially under extreme driving conditions [1–5]. It is featured with short reaction time and strong vehicle instability propensity [6–8]. Trajectory tracking control plays a vital role in ensuring vehicle safety in emergency obstacle avoidance scenarios [9]. Four-wheel-independent-drive electric vehicles (FWID EVs) have the potential to enhance trajectory tracking and vehicle dynamics stability by independently and accurately controlling the drive/brake torque of each wheel [10, 11].

Trajectory tracking control encompasses two primary components: lateral and longitudinal control [9]. The existing trajectory tracking control methods can be generally categorized into decoupled and integrated control architectures. A variety of control algorithms have been employed, including the proportional, integral, and derivative (PID) [12], sliding model control (SMC) [13], linear quadratic regulator (LQR) [14], fuzzy logic [15], robust control [16], model predictive control (MPC) [17], and machine learning-based control [18]. For instance, Chen et al. [19] developed

✉ Xiaolin Ding
xiaolinding@bit.edu.cn; xld_vehicle@163.com

¹ Advanced Technology Research Institute Beijing Institute of Technology, Jinan 250300, China

² Guangzhou Pengxu Autonomous Driving Technology Co. Ltd., Guangzhou 510700, China

³ National Engineering Research Center for Electric Vehicles, Beijing Institute of Technology, Beijing 100081, China

an integrated trajectory tracking controller combining a nonlinear MPC and a barrier function method. In contrast, Lin et al. [20] presented a decoupled control scheme that respectively utilizes MPC and SMC for lateral and longitudinal control. Compared to the integrated approach, the decoupled architecture remarkably reduces the matrix dimension of the objective function, thereby improving computational efficiency. To enhance trajectory tracking accuracy, Xu et al. [21] leveraged torque-vectoring control to compensate for vehicle yaw angle tracking errors while fulfilling the overall driving torque demand. In high-speed emergency obstacle avoidance scenarios, tires usually operate within the transition or saturation region. However, the existing control methods often use a linear tire model to design a trajectory tracking controller, which ignores the impact of tire nonlinear characteristics on vehicle trajectory tracking accuracy. Furthermore, these control schemes improve the accuracy of vehicle trajectory tracking only by adjusting the front-wheel steering angle, while neglecting the potential vehicle yaw instability caused by tire force saturation, which may even lead to severe accidents. Therefore, it is important to ensure yaw stability during vehicle trajectory tracking.

In practical scenarios, conflicts may arise between trajectory tracking and vehicle yaw stability control. Thus, it is imperative to efficiently coordinating the two controllers under different driving conditions. Preliminary studies have been carried out for trajectory tracking and yaw stability coordination, and the existing methods often employ centralized and distributed control architectures. The centralized methods typically encapsulate the stability objectives such as vehicle sideslip angle and yaw rate and the trajectory tracking objectives such as front-wheel steering angle and total longitudinal force as the control variables [22–25]. On this regard, Zhai et al. [22] proposed an integrated control strategy based on MPC to improve trajectory tracking accuracy and handling stability for intelligent four-wheel-independent-drive electric vehicles. Analogously, Cheng et al. [25] proposed a lateral-stability-coordinated collision avoidance control system based on MPC to effectively reduce vehicle collision accidents via four-wheel auto brake. In contrast, the trajectory tracking and yaw stability controllers are independently developed in the distributed control architecture [20, 26–29]. For instance, Xie et al. [30] devised a sliding mode controller by concurrently considering both lateral trajectory tracking and vehicle yaw rate errors through appropriate weighting coefficients. It achieved improved vehicle stability during trajectory tracking control; however, it becomes invalid when the yaw rate is relatively low.

Assessing vehicle stability is crucial for determining when to activate vehicle stability control during trajectory tracking [31]. Current methods for assessing vehicle stability primarily include the Lyapunov method and the phase plane method. The Lyapunov method comprises of the

Lyapunov function method and the Lyapunov exponential method. However, applying the Lyapunov function method in trajectory tracking processes poses challenges due to the necessity of constructing a scalar energy-like function, which is unsuitable for systems with high Degrees of Freedom (DoF) [32]. In comparison, the Lyapunov exponential method [33] gauges the convergence speed of the vehicle's regression stabilization point by establishing a 2-DOF nonlinear dynamics model. This approach provides the quantitative evaluation metrics for vehicle stability assessment [34]. The phase plane method [35], as demonstrated by Bobier-Tiu et al. [36], constructs the yaw stability boundaries by using a 2-DOF vehicle dynamics model. The stability boundaries within the phase plane of the sideslip angle β and yaw rate $\dot{\phi}$ are derived according to the isoline of vehicle state derivatives. Furthermore, the influence of steering and braking on the open-loop dynamics is further elucidated via the closed-loop phase trajectory diagram [37, 38]. These involve with various vehicle parameters such as load transfer, vehicle speed, road adhesion, and front-wheel steering angle to delineate the yaw stability boundaries. However, the phase plane methods often rely on either empirical formulations or preset thresholds, leading to subjective interpretations and unreasonable assumptions.

Previous studies have presented various methods for improving the trajectory tracking accuracy and vehicle yaw stability of automated vehicles. Challenges still remain in how to accurately trigger yaw stability control and efficiently coordinate trajectory tracking and yaw stability control under varying driving conditions. To address these issues, this study proposes an enabling trajectory tracking scheme with improved vehicle yaw stability for FWID EVs. First, a modified phase plane method is developed to evaluate the 3-dimensional phase trajectory for vehicle yaw stability assessment. Then a lateral trajectory tracking controller with a variable stiffness tire model is presented based on model predictive control. A dual-weight distributed cooperative sliding mode control method is presented for the yaw angle tracking compensation and yaw stability control through control objectives switching. Finally, the desired additional yaw moment and total longitudinal tire force are realized through wheel torque allocation while accounting for wheel slip ratios. The performance of the proposed control scheme is validated under high-speed double-lane change maneuvers. The exclusive contributions of this study to the existing literature are summarized as follows:

- A lateral trajectory tracking controller utilizing a variable stiffness tire model is presented based on model predictive control to improve the robustness of trajectory tracking.
- A dual-weight distributed cooperative sliding mode control method is proposed for yaw angle tracking compen-

- sation and yaw stability control through switching the control objectives.
- The stability of the proposed trajectory tracking and stability control scheme is validated through theoretical proofing.

This paper is structured as follows: Sect. 2 presents the system modeling. Section 3 introduces the modified yaw stability assessment method. Section 4 details the proposed cooperative trajectory tracking and stability control scheme. Section 5 presents the hardware-in-the-loop experimental verification, with key conclusions outlined in Sect. 6.

2 System Modeling

2.1 Vehicle Dynamic and Kinematic Models

The research focus of this study is on the trajectory tracking and yaw stability control on a flat road. To simplify the vehicle dynamics model and improve the computational efficiency, the influence of vehicle suspension on vehicle pitch and roll motions are ignored. Thus, a single-track 3-DOF vehicle dynamics model is adopted to characterize vehicle longitudinal, lateral, and yaw motions, as shown in Fig. 1. The following assumptions are made: (1) The origin of the vehicle coordinate system coincides with the vehicle's Center of Gravity (CoG); (2) The vehicle vertical, pitch, and roll motions are negligible; (3) The vehicle is symmetrical with respect to the xoz plane; (4) The influence of the suspension on vehicle motions is negligible [39]. It should be noted that the suspension effect needs to be considered when driving on off-road surfaces or when assessing the influence of vehicle roll and pitch motions on vehicle stability in emergency scenarios. The 3-DOF vehicle dynamics model is given by

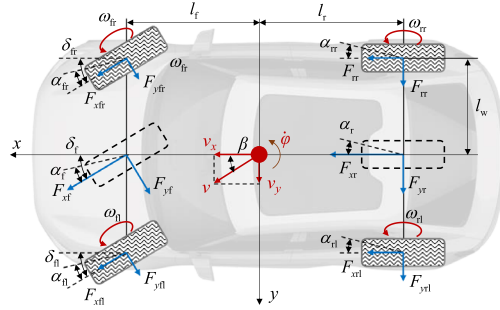


Fig. 1 Vehicle dynamics model

$$\begin{cases} m(\dot{v}_x - v_y \dot{\varphi}) = F_{xf} \cos \delta_f - F_{yr} \sin \delta_f + F_{xr} + F_r \\ m(\dot{v}_y + v_x \dot{\varphi}) = F_{xf} \sin \delta_f + F_{yr} \cos \delta_f + F_{yr} \\ I_{zz} \ddot{\varphi} = (F_{xf} \sin \delta_f + F_{yr} \cos \delta_f) l_f - F_{yr} l_r \end{cases} \quad (1)$$

where m is the vehicle mass; v_x and v_y are the vehicle longitudinal and lateral velocities; $\dot{\varphi}$ is the yaw rate; φ is the yaw angle; δ_f is the front-wheel steering angle; I_{zz} is the vehicle moment of inertia around the z -axis; l_f and l_r are the distances between CoG and the front and rear axles, respectively; F_{xf} and F_{xr} are the longitudinal tire forces at the front and rear axles, respectively; F_{yr} and F_{yr} are the lateral tire forces at the front and rear axles, respectively; F_r is the overall driving resistance, which is given by

$$F_r = F_a + F_g + F_\omega \quad (2)$$

where F_g is the grade resistance; F_a is the air resistance; F_ω is the rolling resistance. Here, the road gradient is assumed to be zero resulting in $F_g = 0$.

The vertical force at each wheel is given by

$$\begin{cases} F_{zfl} = \frac{mgl_f}{2(l_f+l_r)} + \frac{mh_g(-a_x l_w - a_y l_r)}{2(l_f+l_r)l_w} \\ F_{zfr} = \frac{mgl_f}{2(l_f+l_r)} + \frac{mh_g(-a_x l_w + a_y l_r)}{2(l_f+l_r)l_w} \\ F_{zrl} = \frac{mgl_f}{2(l_f+l_r)} + \frac{mh_g(a_x l_w - a_y l_r)}{2(l_f+l_r)l_w} \\ F_{zrr} = \frac{mgl_f}{2(l_f+l_r)} + \frac{mh_g(a_x l_w + a_y l_r)}{2(l_f+l_r)l_w} \end{cases} \quad (3)$$

where F_{zij} is the vertical force at each wheel with $i \in \{f, r\}$ and $j \in \{l, r\}$ representing the front and rear and the left and right; h_g is the height of CoG; l_w is the half of the wheel track; a_x and a_y are the vehicle longitudinal and lateral accelerations, respectively; g is the gravitational acceleration.

Both the wheel slip angle and slip ratio are important for calculating the wheel's longitudinal and lateral forces. The wheel slip angle α_{ij} is given by

$$\begin{cases} \alpha_{fl} = \arctan \left(\frac{v_y + l_f \dot{\varphi}}{v_x - l_w \dot{\varphi}} \right) - \delta_f, \alpha_{rl} = \arctan \left(\frac{v_y - l_r \dot{\varphi}}{v_x - l_w \dot{\varphi}} \right) \\ \alpha_{fr} = \arctan \left(\frac{v_y + l_f \dot{\varphi}}{v_x + l_w \dot{\varphi}} \right) - \delta_f, \alpha_{rr} = \arctan \left(\frac{v_y - l_r \dot{\varphi}}{v_x + l_w \dot{\varphi}} \right) \end{cases} \quad (4)$$

The slip ratio κ_{ij} is given by

$$\kappa_{ij} = \begin{cases} \frac{\omega_{ij} R_w - v_{ij}}{\omega_{ij} R_w}, \omega_{ij} R_w > v_{ij} \\ \frac{v_{ij} - \omega_{ij} R_w}{v_{ij}}, \omega_{ij} R_w \leq v_{ij} \end{cases} = -k_s \left(\left(\frac{v_x}{\omega_{ij} R_w} \right)^{k_s} - 1 \right) \quad (5)$$

where v_{ij} is the vehicle longitudinal velocity at the wheel; R_w and ω_{ij} are the effective rolling radius and rotational speed;

k_s is the sign of the tire's slip state. When $\omega_{ij}R_w > v_{ij}$, k_s is 1; conversely, k_s is -1.

2.2 Tire Model

Using a linear tire model like the Brush model cannot accurately describe tire forces as it assumes a fixed tire stiffness and connects the tire to the ground through small flexible brush units. There would be significant modeling errors when the tire enters in the saturation region. In this study, a tire stiffness model is developed by using the Pacejka tire model and the cutoff method [40]. It combines the vertical load, road friction coefficient, and tire slip state for each tire to calculate the tire stiffness through the linear interpolation, which is given by

$$F_t = D_t \sin(C_t \arctan(B_t x_t - E_t(B_t x_t - \arctan(B_t x_t)))) \quad (6)$$

where F_t is the tire force; x_t is the tire slip state; B_t , C_t , D_t , and E_t are the parameters of the Pacejka tire model and are subject to the road adhesion μ and the vertical tire force F_{zij} .

Based on Eq. (6), the tire stiffness can be obtained by the lookup table $C_k(x_t, \mu, F_{zij}) = F_t/x_t$, where $k \in \{x, y\}$ is the longitudinal or lateral direction. The tire forces can be approximately calculated by

$$\begin{aligned} F_{xij} &= C_x(\kappa_{ij}, \mu, F_{zij})\kappa_{ij} \\ F_{yij} &= C_y(\alpha_{ij}, \mu, F_{zij})\alpha_{ij} \end{aligned} \quad (7)$$

The 3-DoF vehicle dynamics model can be given by

$$\begin{cases} \dot{v}_x = v_y \dot{\phi} + \frac{1}{m}(C_{xf}\kappa_f \cos \delta_f - C_{yf}\alpha_f \sin \delta_f + C_{xr}\kappa_r) \\ \dot{v}_y = -v_x \dot{\phi} + \frac{1}{m}(C_{xf}\kappa_f \sin \delta_f + C_{yf}\alpha_f \cos \delta_f + C_{yr}\alpha_r) \\ \ddot{\phi} = \frac{1}{I_{zz}}((C_{xf}\kappa_f \sin \delta_f + C_{yf}\alpha_f \cos \delta_f)l_f - C_{yr}\alpha_r l_r) \end{cases} \quad (8)$$

where C_{xf} and C_{xr} are the longitudinal tire stiffness at the front and rear axles; C_{yf} and C_{yr} are the lateral tire stiffness at the front and rear axles; κ_f and κ_r are the average slip ratios of the front and rear wheels; α_f and α_r are the average effective tire slip angles at the front and rear axles.

2.3 Trajectory Tracking Model

Figure 2 illustrates the relationship between the vehicle and the reference trajectory in the global coordinate system. ψ is the vehicle heading angle; v_x is the velocity in the X direction; X_h and Y_h are the host vehicle's locations in the X and Y direction, respectively; ref is the reference state; e_Y , e_ψ , e_φ and e_{v_x} are the errors of the lateral distance in the Y direction, heading angle, yaw angle and velocity in the X direction, respectively. In particular, $e_\psi = e_\varphi$.

Define $\mathbf{x} = [v_x, v_y, \varphi, \dot{\phi}, X_h, Y_h]^T$ as the state vector, $u = \delta_f$ as the control variable, $\mathbf{y} = [Y_h, \varphi]^T$ as the system output,

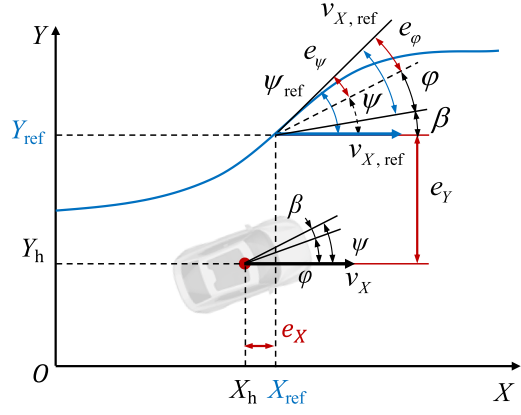


Fig. 2 Illustration of the trajectory tracking error

and $\mathbf{w} = [F_r, 0, 0, 0, 0]^T$ as the disturbance. The equations of trajectory tracking are given by

$$\begin{cases} \dot{\mathbf{x}} = \mathbf{Ax} + \mathbf{Bu} + \mathbf{w} \\ \mathbf{y} = \mathbf{Cx} \end{cases} \quad (9)$$

where

$$\mathbf{A} = \begin{bmatrix} a_{11} & a_{12} & 0 & a_{14} & 0 & 0 \\ a_{21} & a_{22} & 0 & a_{24} & 0 & 0 \\ 0 & 0 & 0 & 1 & 0 & 0 \\ a_{41} & a_{42} & 0 & a_{44} & 0 & 0 \\ a_{51} & a_{52} & a_{53} & 0 & 0 & 0 \\ a_{61} & a_{62} & a_{63} & 0 & 0 & 0 \end{bmatrix}, \mathbf{B} = \begin{bmatrix} b_{11} \\ b_{21} \\ 0 \\ b_{41} \\ 0 \\ 0 \end{bmatrix},$$

$$\mathbf{C} = \begin{bmatrix} 0 & 0 & 0 & 0 & 0 & 1 \\ 0 & 0 & 1 & 0 & 0 & 0 \end{bmatrix}$$

$$a_{11} = -\frac{C_{xf} \cos \delta_f k_f^2 q_f^{k_s} + C_{yf} \sin \delta_f p_f + C_{xr} k_r^2 q_r^{k_s}}{mv_x},$$

$$a_{12} = \dot{\phi} + \frac{C_{yf} \sin \delta_f}{mv_x}, a_{14} = v_y + \frac{l_f C_{yf} \sin \delta_f}{mv_x},$$

$$a_{21} = -\dot{\phi} + \frac{-C_{xf} \sin \delta_f k_f^2 q_f^{k_s} + C_{yf} \cos \delta_f p_f + C_{yr} p_r}{mv_x},$$

$$a_{22} = -\frac{C_{yf} \cos \delta_f + C_{yr}}{mv_x}, a_{24} = -v_x + \frac{-l_f C_{yf} \cos \delta_f + l_r C_{yr}}{mv_x},$$

$$a_{41} = \frac{l_f (-C_{xf} \sin \delta_f k_f^2 q_f^{k_s} + C_{yf} \cos \delta_f p_f) - l_r C_{yr} p_r}{I_{zz} v_x},$$

$$a_{42} = -\frac{l_f C_{yf} \cos \delta_f + l_r C_{yr}}{I_{zz} v_x}, a_{44} = -\frac{l_f^2 C_{yf} \cos \delta_f + l_r^2 C_{yr}}{I_{zz} v_x},$$

$$a_{51} = \cos \varphi, a_{52} = -\sin \varphi, a_{53} = -v_x \sin \varphi - v_y \cos \varphi,$$

$$a_{61} = \sin \varphi, a_{62} = \cos \varphi, a_{63} = v_x \cos \varphi - v_y \sin \varphi,$$

$$b_{11} = \frac{C_{xf} \sin \delta_f k_f (q_f^{k_s} - 1) - C_{yf} (\cos \delta_f (\delta_f - p_f) + \sin \delta_f)}{m}$$

$$b_{21} = -\frac{C_{xf} \cos \delta_f k_f (q_f^{k_s} - 1) + C_{yf} (\sin \delta_f (\delta_f - p_f) - \cos \delta_f)}{m}$$

$$b_{41} = -\frac{l_f (C_{xf} \cos \delta_f k_f (q_f^{k_s} - 1) + C_{yf} (\sin \delta_f (\delta_f - p_f) - \cos \delta_f))}{I_{zz}}$$

$$p_f = \frac{v_y + l_f \dot{\varphi}}{v_x}, p_r = \frac{v_y - l_f \dot{\varphi}}{v_x}, q_f = \frac{v_x}{R_w \omega_f}, q_r = \frac{v_x}{R_w \omega_r}$$

Define the reference velocity $v_{X,\text{ref}}$ in the X direction, and the velocity error can be given by

$$e_{v_X} = v_X - v_{X,\text{ref}} = (v_x \cos \varphi - v_y \sin \varphi) - v_{X,\text{ref}} \quad (10)$$

where e_{v_X} is the velocity error; $v_{X,\text{ref}}$ is the reference velocity.

The derivative of the velocity error is calculated by

$$\dot{e}_{v_X} = \dot{v}_X - \dot{v}_{X,\text{ref}} = (\dot{v}_x \cos \varphi - \dot{v}_y \sin \varphi) - \dot{v}_{X,\text{ref}} \quad (11)$$

3 Modified Vehicle Yaw Stability Criterion

Accurate assessment of vehicle dynamics stability is essential for the effective activation of yaw stability control. This study expands the traditional two-dimensional phase plane into a three-dimensional phase space by incorporating the vehicle's longitudinal motion, thereby enabling a more precise evaluation of the vehicle's yaw stability.

Based on the 3-DOF vehicle dynamics model described in Eq. (1), vehicle parameters including vehicle dimensions and mass distribution have an effect on system stability, but can be generally considered to be fixed over the duration of a single vehicle trip, thereby the tire properties are the main factors affecting the shape of the phase plane.

Assuming that the front-wheel steering angle remains constant and the longitudinal force is zero within the specified time duration, the tire lateral force primarily depends on the tire slip angle. The tire slip angle of each wheel can be calculated based on Eq. (4), and the tire cornering stiffness

under different tire angles, vertical loads, and road friction coefficients can be obtained through a table lookup. It should be noted that a larger tire lateral stiffness results in a wider stable region.

By substituting tire cornering stiffness into Eq. (1), the vehicle phase trajectory can be plotted at different initial lateral velocities, longitudinal velocities, yaw rates, front-wheel steering angles, and road friction coefficients. The first-order forward Euler method is used to discretize the 3-DOF state space equation, and the $v_y - \dot{\varphi} - v_x$ phase trajectories within a certain time domain are iteratively calculated using MATLAB to achieve phase trajectory visualization.

The definition of the stability criterion is given as follows: once the $v_y - \dot{\varphi} - v_x$ phase plane has been obtained, the vehicle stability state can be determined by assessing whether the phase trajectory converges to an equilibrium point.

Under the condition of $v_x = 20$ m/s, $\mu = 0.8$ and $\delta_f = -5^\circ$, the phase trajectory in Fig. 3 is analyzed under different initial states, which is given as follows:

- (1) Where the initial values of v_y and $\dot{\varphi}$ are small, like t4 and t7, the $v_y - \dot{\varphi}$ phase trajectory shows prominent equilibrium points, with relatively small variation in v_x .
- (2) The equilibrium points of t2 and t5 are also evident in the $v_y - \dot{\varphi}$ phase trajectory but with drastic changes in v_x and v_y , resulting in significant vehicle speed increase or decrease.
- (3) The $v_y - \dot{\varphi}$ phase trajectory of t8 fails to reach a steady state within a long time frame (5 s), exhibiting severe oversteer characteristics and entering a spin state, with substantial increases in v_y and $\dot{\varphi}$ while the vehicle speed v remains constant. For converging phase trajectories, they eventually converge to a curved "stem", similar to the stable points in the $v_y - \dot{\varphi}$ phase plane [41]. Based on this feature, the phase plane can be separated into the 'stable' and 'unstable' areas as shown in Fig. 4.

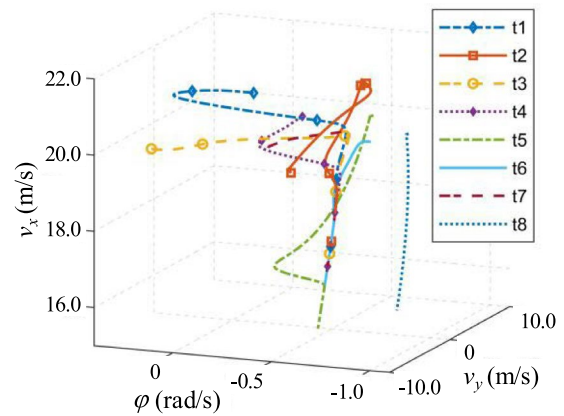


Fig. 3 Phase trajectories for different initial states

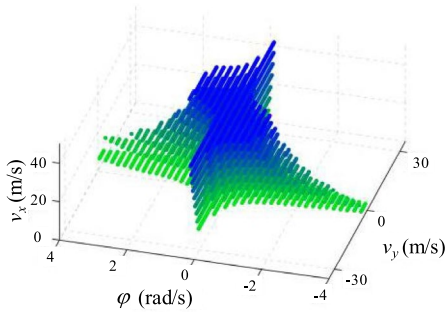


Fig. 4 Stable region division

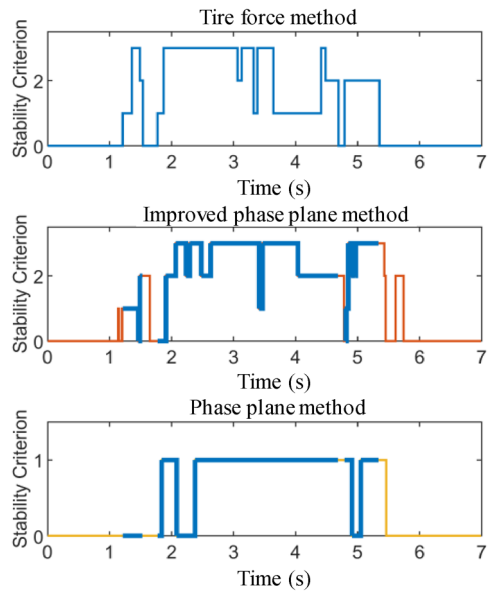


Fig. 5 Comparison of different vehicle stability assessment methods

Because of the impact of dramatic sideslip angle changes on driver mentality and tire force utilization, a constraint on the sideslip angle is imposed based on the tire-road adhesion ellipse. In the stable region, when the phase trajectories do not satisfy the constraints, the initial state is considered unstable; conversely, it is regarded as stable. The constraint on the sideslip angle is given by

$$\beta_{\max} = \frac{l_s \phi}{v_x} + \tan(\alpha_{sl}), \quad \beta_{\min} = \frac{l_s \phi}{v_x} - \tan(\alpha_{sl}) \quad (12)$$

where β_{\max} and β_{\min} are the maximum and minimum sideslip angles, respectively; α_{sl} is the tire slip angle that corresponds to the tire's peak force.

Using the phase plane method as a comparison method, the performance of the modified yaw stability assessment method is verified in Sect. 6. According to the assessment results presented in Fig. 5, the modified phase plane method exhibits higher accuracy compare to the traditional phase

plane method. Further analyzing the impacts of vehicle speed, road adhesion, and front-wheel steering angle on stability boundaries reveals similar trends in the $v_y - \phi$ phase plane as observed in Ref. [38]. As the vehicle speed increases from 5 to 45 km/h, the stability boundaries expand in the v_y direction and contracts in the ϕ direction. As the road friction coefficient increases from 0.1 to 1, the stability boundaries expand in the v_y and ϕ directions. As the front-wheel steering angle increases from 0 to 0.4 rad, the stability boundaries shift from the bottom right-hand to the top left-hand side. Unlike the 2-D phase plane, when the front-wheel steering angle is non-zero, the stability boundaries change, with the stable points shifting relatively upward and to the left, which is no longer symmetrical about the stable points.

4 Cooperative Trajectory Tracking and Stability Control

The schematic of the proposed cooperative trajectory tracking and stability control scheme is illustrated in Fig. 6. The motion planning layer generates a reference trajectory based on environmental perception and vehicle states. The lateral trajectory tracking controller calculates the front-wheel steering angle δ_f . In the yaw stability control module, a modified phase plane method is developed for vehicle dynamics stability assessment. Taking into account the yaw stability state SI and yaw angle tracking error $e_{\varphi s}$, a dual-weight cooperative yaw moment ΔM_z controller is put forward for yaw angle tracking compensation and yaw stability control through the adaptive adjustment of q_t and q_s . For the longitudinal velocity tracking, an SMC method is also utilized to obtain total longitudinal force to track the reference vehicle longitudinal velocity. The torque distribution module can optimally allocate the driving/braking torque for each wheel to realize the total longitudinal force and additional yaw moment while accounting for the tire slip ratio.

4.1 Lateral Trajectory Tracking Controller

An MPC-based controller is developed to realize lateral trajectory tracking. Discrete controller formulations with a time-varying tire stiffness model are derived using the forward Euler method by balancing model accuracy and computational efficiency. Compared with the fixed tire stiffness model, the used time-varying tire stiffness model has high accuracy in the tire's saturation region. The discrete state equations are given by

$$\begin{cases} \mathbf{x}_{k+1} = \mathbf{A}_k \mathbf{x}_k + \mathbf{B}_k u_k + T_p \mathbf{w}_k \\ \mathbf{y}_k = \mathbf{C}_k \mathbf{x}_k \end{cases} \quad (13)$$

where T_p is the discrete time period, and $\mathbf{A}_k = \mathbf{A}(t, k)T_p + \mathbf{I}_{6 \times 6}$, $\mathbf{B}_k = \mathbf{B}(t, k)T_p$, and $\mathbf{C}_k = \mathbf{C}(t, k)$ are also defined at the k -th sampling time.

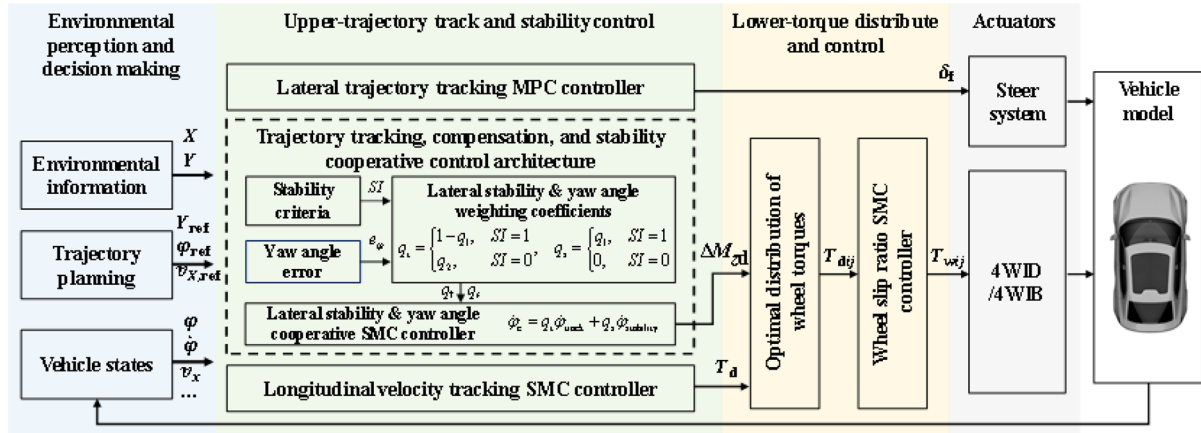


Fig. 6 Schematic of the proposed cooperative trajectory tracking and stability control scheme

Combine the system states \mathbf{x} and the input variable u to form an extended state vector as

$$\xi = \begin{bmatrix} \mathbf{x}_k \\ u_{k-1} \end{bmatrix} \quad (14)$$

Thus, the discrete state equations with the extended state vector are derived as

$$\begin{cases} \xi_{k+1} = A_d \xi_k + B_d \Delta u_k + T_p \tilde{\mathbf{w}}_k \\ y_k = C_d \xi_k \end{cases} \quad (15)$$

where $\Delta u_k = u_k - u_{k-1}$ is the control increment; $\tilde{\mathbf{w}}_k = [\mathbf{w}_k \ 0]^T$ is the extended disturbance with A_d, B_d, C_d defined as

$$A_d = \begin{bmatrix} A_k & B_k \\ \mathbf{0}_{1 \times 6} & 1 \end{bmatrix}, B_d = \begin{bmatrix} B_k \\ 1 \end{bmatrix}, C_d = \begin{bmatrix} C_k^T \\ 0 \end{bmatrix}^T \quad (16)$$

Assuming that the coefficient matrix is constant within the prediction horizon N_p , the extended state vector within N_p can be iteratively calculated by

$$\begin{aligned} \xi_{k+1} &= A_d \xi_k + B_d \Delta u_k + T_p \tilde{\mathbf{w}}_k \\ \xi_{k+2} &= A_d^2 \xi_k + A_d (B_d \Delta u_k + T_p \tilde{\mathbf{w}}_k) + B_d \Delta u_{k+1} + T_p \tilde{\mathbf{w}}_{k+1} \\ &\dots \\ \xi_{k+N_c} &= A_d^{N_c} \xi_k + A_d^{N_c-1} (B_d \Delta u_k + T_p \tilde{\mathbf{w}}_k) \\ &\quad + \dots + B_d \Delta u_{k+N_c-1} + T_p \tilde{\mathbf{w}}_{k+N_c-1} \\ &\dots \\ \xi_{k+N_p} &= A_d^{N_p} \xi_k + A_d^{N_p-1} (B_d \Delta u_k + T_p \tilde{\mathbf{w}}_k) \\ &\quad + \dots + A_d^{N_p-N_c} (B_d \Delta u_{k+N_c-1} + T_p \tilde{\mathbf{w}}_{k+N_c-1}) \\ &\quad + A_d^{N_p-N_c-1} T_p \tilde{\mathbf{w}}_{k+N_c} + \dots + T_p \tilde{\mathbf{w}}_{k+N_p-1} \end{aligned} \quad (17)$$

Similarly, the output vector y within N_p also has an approximate expression. The system outputs \mathbf{Y}_A within the prediction horizon can be represented by the extended state vector ξ at moment k , the control increment vector in the control horizon ΔU , and the disturbance vector in the prediction horizon W . The state-space equation is given by

$$\mathbf{Y}_A = \Psi \xi_k + \Theta \Delta U + \Omega W \quad (18)$$

where

$$\begin{aligned} \mathbf{Y}_A &= \left[\mathbf{y}_{k+1} \ \mathbf{y}_{k+2} \ \dots \ \mathbf{y}_{k+N_c} \ \dots \ \mathbf{y}_{k+N_p} \right]^T, \\ \Delta U &= \left[\Delta u_k \ \Delta u_{k+1} \ \dots \ \Delta u_{k+N_c-1} \right]^T, \\ W &= \left[\tilde{\mathbf{w}}_k \ \tilde{\mathbf{w}}_{k+1} \ \dots \ \tilde{\mathbf{w}}_{k+N_p-1} \right]^T, \\ \Psi &= \left[C_d A_d \ C_d A_d^2 \ \dots \ C_d A_d^{N_c} \ \dots \ C_d A_d^{N_p} \right]^T, \\ \Theta &= \left[\begin{array}{cccc} C_d B_d & 0 & \dots & 0 \\ C_d A_d B_d & C_d B_d & \dots & 0 \\ \vdots & \vdots & \ddots & \vdots \\ C_d A_d^{N_c-1} B_d & C_d A_d^{N_c-2} B_d & \dots & C_d B_d \\ \vdots & \vdots & \ddots & \vdots \\ C_d A_d^{N_p-1} B_d & C_d A_d^{N_p-2} B_d & \dots & C_d A_d^{N_p-N_c} B_d \end{array} \right], \\ \Omega &= \left[\begin{array}{cccc} C_d T_p & 0 & \dots & 0 \\ C_d A_d T_p & C_d T_p & \dots & 0 \\ \vdots & \vdots & \ddots & 0 \\ C_d A_d^{N_c-1} T_p & C_d A_d^{N_c-2} T_p & \dots & 0 \\ \vdots & \vdots & \ddots & 0 \\ C_d A_d^{N_p-1} T_p & C_d A_d^{N_p-2} T_p & \dots & C_d T_p \end{array} \right] \end{aligned}$$

The objective function is defined as

$$\begin{aligned}
J &= (\mathbf{Y}_A - \mathbf{Y}_{A,\text{ref}})^T \mathbf{Q}_A (\mathbf{Y}_A - \mathbf{Y}_{A,\text{ref}}) + \Delta \mathbf{U} \mathbf{R}_A \Delta \mathbf{U} \\
&= \Delta \mathbf{U}^T (\Theta^T \mathbf{Q}_A \Theta + \mathbf{R}_A) \Delta \mathbf{U} + 2(\mathbf{E}^T \mathbf{Q}_A \Theta \\
&\quad - \mathbf{Y}_{A,\text{ref}}^T \mathbf{Q}_A \Theta) \Delta \mathbf{U} \\
&\quad + \underbrace{\mathbf{E}^T \mathbf{Q}_A \mathbf{E} + \mathbf{Y}_{A,\text{ref}}^T \mathbf{Q}_A \mathbf{Y}_{A,\text{ref}} - 2 \mathbf{Y}_{A,\text{ref}}^T \mathbf{Q}_A \mathbf{E}}_{\text{Constant}}
\end{aligned} \tag{19}$$

where $\mathbf{E} = \Psi \xi_k + \Omega \mathbf{W}$; $\mathbf{Y}_{A,\text{ref}}$ is the reference output within N_p ; \mathbf{Q}_A and \mathbf{R}_A are the weighting coefficient matrices of the system output within N_p , and the input within N_c , respectively. A larger \mathbf{Q}_A indicates that the control input tracks system control objectives as closely as possible, and a larger \mathbf{R}_A indicates an expected smooth control movement to prevent excessive control input.

Considering the actuators' characteristics, the constraints are given by

$$\begin{aligned}
u_{\min} \leq u \leq u_{\max} \\
\Delta u_{\min} \leq \Delta u \leq \Delta u_{\max}
\end{aligned} \tag{20}$$

where u_{\min} and u_{\max} are the minimal and maximal steering angles of the front-wheel; Δu_{\min} and Δu_{\max} are the minimum and maximum front-wheel steering angle increments.

In order to prevent the front tires from entering into the saturation region, a constraint on the front-wheel steering angle is given by

$$\arctan \frac{\alpha_{f,\min} + l_f \phi}{v_x} \leq \alpha_f \leq \arctan \frac{\alpha_{f,\max} + l_f \phi}{v_x} \tag{21}$$

where $\alpha_{f,\min}$ and $\alpha_{f,\max}$ represent the minimum and maximum sideslip angles that correspond to the peak tire force.

The MPC-based trajectory tracking controller can be reformulated as a quadratic programming problem, which is given by

$$\min J = \frac{1}{2} \Delta \mathbf{U} \mathbf{H}_A \Delta \mathbf{U}^T + \mathbf{f}_A^T \Delta \mathbf{U} \tag{22}$$

where $\mathbf{H}_A = \Theta^T \mathbf{Q}_A \Theta + \mathbf{R}_A$ and $\mathbf{f}_A = \Theta^T \mathbf{Q}_A (\mathbf{E} - \mathbf{Y}_{\text{ref}})$.

By using a quadratic programming algorithm to solve the optimization problem, the optimal control increment sequence $\Delta \mathbf{U}$ can be obtained.

4.2 Yaw Stability and Yaw Angle Compensation Controller

The yaw stability control system takes the steady-state value of the yaw rate during a constant steering maneuver as its control objective. This is commonly employed to characterize the stable vehicle state. In contrast, the yaw angle error compensation control takes the yaw angle of the reference trajectory and the yaw rate as the control objective, which

reflects the vehicle's maneuverability performance. Both are motion controls in the direction of yaw, so a controller can be constructed to realize both yaw stability control and yaw angle error compensation control to simplify the controller structure.

- (1) The control objective of the yaw stability controller: Based on the vehicle's yaw dynamics equation and the Laplace transform, the expected value of the vehicle reference steady-state yaw rate is given by

$$\dot{\phi}_{ss} = G_\phi \delta_f \tag{23}$$

where

$$G_\phi = \frac{v_x(l_f + l_r)C_{yf}C_{yr}}{(l_f + l_r)^2 C_{yf}C_{yr} + mv_x^2(-l_f C_{yf} + l_r C_{yr})}$$

Considering the impact of road adhesion on tire force limits, the desired vehicle yaw rate should satisfy

$$\dot{\phi}_{\text{stability}} = \text{sign}(\dot{\phi}_{ss}) \min \{ |\dot{\phi}_{ss}|, \dot{\phi}_0 \} \tag{24}$$

- where $\dot{\phi}_0 = \mu g / v_x$
- (2) The control objective of the compensation controller: The control target of the compensation controller is the reference trajectory's yaw angle ϕ_{track} .
- (3) Switch SMC Controller Design: SMC has been widely adopted for generating the desired additional yaw moment. Combining the aforementioned control objectives, the sliding mode surface is given by

$$s_B = e_\phi + \dot{e}_\phi = (\varphi - \varphi_d) + (\dot{\varphi} - \dot{\varphi}_d) \tag{25}$$

where e_ϕ denotes the yaw angle error; φ_d represents the desired yaw angle.

Introducing the additional yaw moment ΔM_z into the yaw motion, the differential equation can be given by

$$\ddot{\varphi} = -\frac{l_f C_f - l_r C_r}{I_{zz}} \beta - \frac{l_f^2 C_f + l_r^2 C_r}{I_{zz} v_x} \dot{\varphi} + \frac{l_f C_f}{I_{zz}} \delta_f + \frac{\Delta M_z}{I_{zz}} \tag{26}$$

An appropriate sliding mode reaching law can strike a balance in reducing chattering phenomenon and improving algorithm convergence rate. The exponential reaching law is used in this study, which is given by

$$\dot{s}_B = -\epsilon_B \text{sign}(s_B) - k_B s_B, \epsilon_B > 0, k_B > 0 \tag{27}$$

where $\epsilon_B \text{sign}(s_B)$ is the constant-speed convergence term; $k_B s_B$ is the exponential convergence term. When ϵ_B is large, the exponential term plays the major role, and the exponential level decreases with the increasing ϵ_B ; when ϵ_B is small, the sliding mode surface is approximately approached at a

constant rate. Small ε_B and large k_B can increase the convergence rate while reducing the chattering phenomenon.

Combining Eqs. (27) and (26), the desired additional yaw moment $\Delta M_{z,\text{des}}$ can be derived as

$$\Delta M_{z,\text{des}} = I_{zz} \left(\frac{l_f C_f - l_r C_r}{I_{zz}} \beta + \frac{l_f^2 C_f + l_r^2 C_r}{I_{zz} v_x} \dot{\varphi} - \frac{l_f C_f \delta_f}{I_{zz}} \right) (28)$$

$$+ I_{zz} (\ddot{\varphi}_d - c(\dot{\varphi} - \dot{\varphi}_d) - \varepsilon_B \text{sign}(s_B) - k_B s_B)$$

4.3 Cooperative Trajectory Tracking and Stability Control

The stability criteria module is used to assess the vehicle yaw stability based on current vehicle states. If the vehicle is in an unstable state, the yaw stability control is triggered; otherwise, the yaw angle compensation control is triggered. The switching mechanism between yaw angle error compensation control and yaw stability control is shown in Fig. 7. To reduce the impact of controller intervention, a comprehensive cooperative control strategy is proposed as follows:

The yaw rate control objective is given by

$$\dot{\varphi}_c = q_t \dot{\varphi}_{\text{track}} + q_s \dot{\varphi}_{\text{stability}} \quad (29)$$

where q_t and q_s are the dual adjustment, including the stability adjusting coefficients q_1 and the error compensation adjusting coefficients q_2 . A larger q_t indicates that the additional yaw moment tends to reduce trajectory tracking error, while a larger q_s indicates a tendency to improve yaw stability.

$$q_t = \begin{cases} 1 - q_1, & SI = 1 \\ q_2, & SI = 0 \end{cases}, \quad q_s = \begin{cases} q_1, & SI = 1 \\ 0, & SI = 0 \end{cases} \quad (30)$$

where SI is the stability index, with $SI = 0$ stable state and $SI = 1$ unstable state.

Stability adjustment is determined by the vehicle's yaw rate and tire utilization ratio, with their proportions being adjusted using the weighting index λ . If $0 \leq \lambda \leq \lambda_0$, both the trajectory tracking compensation and yaw stability control are considered; if $\lambda > \lambda_0$, stability control takes priority over trajectory tracking compensation.

$$q_1 = \begin{cases} \frac{e^\lambda - 1}{e^{\lambda_0} - 1}, & 0 \leq \lambda \leq \lambda_0 \\ 1, & \lambda > \lambda_0 \end{cases} \quad (31)$$

where λ_0 is the threshold value set as 2.5.

$$\lambda = \sqrt{p(\frac{\dot{\varphi}}{\dot{\varphi}_0})^2 + \frac{1}{4} \sum \frac{F_{xij}^2 + F_{yij}^2}{(\mu F_{zij})^2}} \quad (32)$$

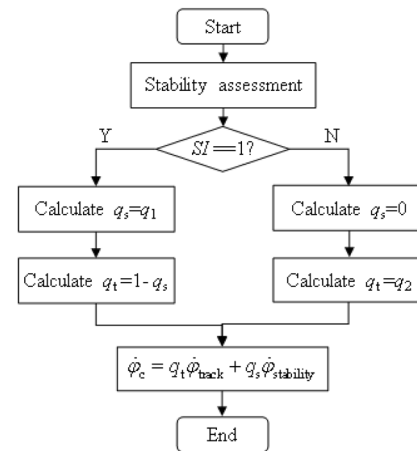


Fig. 7 Comparison of different vehicle stability assessment methods

where p is the weighting adjustment coefficient set as 2. The relationship between adjusting coefficient q_1 and power factor λ is shown in Fig. 8.

To avoid undesirable intervention of the compensation module when the trajectory tracking error is small, the intervention conditions for triggering the compensation control are established using q_2 , and a fifth-order polynomial is formulated to ensure smooth intervention and exiting.

$$q_2 = \begin{cases} 0, & |e_\varphi| \leq e_{s\varphi} \\ \sum_{i=0}^5 a_i (|e_\varphi| - e_{s\varphi})^i, & e_{s\varphi} < |e_\varphi| \leq e_{e\varphi} \\ 1, & |e_\varphi| > e_{e\varphi} \end{cases} \quad (33)$$

where a_i is the weighting coefficient; $|e_{s\varphi}|$ is the maximum error of e_φ when the compensation control is not activated; $|e_{e\varphi}|$ is the minimum error of e_φ when the compensation control is active. The relationship between adjusting coefficient q_2 and yaw angle error e_φ is shown in Fig. 9

4.4 Longitudinal Velocity Tracking Controller

The sliding mode surface can be designed as

$$s_D = e_{v_x}, \quad \dot{s}_D = \dot{e}_{v_x} \quad (34)$$

According to Eq. (8), ignoring the total driving resistance, the global vehicle model in the X -direction can be obtained as

$$m(a_x \cos \varphi - a_y \sin \varphi) = \left(\sum F_x + \Delta F_x \right) \cos \varphi - \sum F_y \sin \varphi \quad (35)$$

$$\text{where } a_x = \dot{v}_x - v_y \dot{\varphi}, \quad a_y = \dot{v}_y + v_x \dot{\varphi},$$

$$\sum F_x = F_{xf} \cos \delta_f - F_{yf} \sin \delta_f + F_{xr},$$

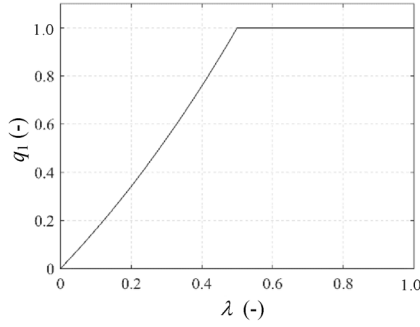


Fig. 8 The relationship between adjusting coefficient q_1 and power factor λ

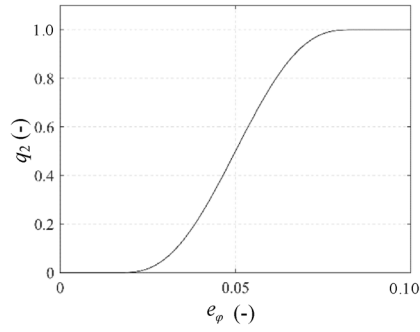


Fig. 9 The relationship between adjusting coefficient q_2 and yaw angle error e_φ

$\sum F_y = F_{xf} \sin \delta_f + F_{yf} \cos \delta_f + F_{yr}$, ΔF_x denotes the longitudinal tire force.

The reaching law presented in Eq. (27) is employed for SMC controller design. The desirable longitudinal tire force can be derived as

$$\begin{aligned} \Delta F_{x,\text{des}} &= \frac{1}{\cos \varphi} \left(- \sum F_{xij} \cos \varphi + \sum F_{yij} \sin \varphi \right. \\ &\quad \left. + m(\dot{v}_{X,\text{ref}} - \dot{\varphi}(v_x \sin \varphi + v_y \cos \varphi) - \varepsilon_D \text{sign}(s_D) - k_D s_D) \right) \end{aligned} \quad (36)$$

where ε_D and k_D are the coefficients of the constant-speed convergence term and the exponential convergence term, respectively.

4.5 Optimal Distribution of Wheel Torques and Wheel Slip Ratio Control

The additional yaw moment output from the yaw stability controller and the total longitudinal tire force from the longitudinal velocity tracking controller are taken as the inputs to the wheel torque distribution module. Through the slip ratio control algorithm, $|\kappa_{ij}|$ is regulated within 0.1. Assuming $\Delta\omega_w \approx 0$, according to the single-wheel vehicle dynamics model, the total drive or brake torque at each wheel can be approximated as

$$I_w \dot{\omega}_{ij} = -F_{xij} R_w + T_{ij} \quad (37)$$

$$T_{ij} = F_{xij} R_w \quad (38)$$

where I_w represents the wheel's moment of inertia; T_{ij} denotes the drive/brake torque of each wheel. Therefore, the desirable equivalent torque T_{des} corresponding to the desirable longitudinal control force is derived as $\Delta F_{x,\text{des}} R_w$.

To minimize the tire load, an objective function is constructed as

$$\min J = Q_E (\Delta M_{z,\text{real}} - \Delta M_{z,\text{des}})^2 + R_E \sum \frac{T_{ij}^2}{(\mu F_{zij} R_w)^2} \quad (39)$$

where $\Delta M_{z,\text{real}}$ is the real additional yaw moment generated by the optimal distribution of wheel torques; Q_E represents the weight of additional yaw moment, and the larger Q_E , the more the control system is expected to track the yaw moment as much as possible; R_E represents the weight of tire utilization rate, with a larger value indicating that the road adhesion utilization rate should be minimized as much as possible during wheel torque allocation; ρ represents the relaxation factor.

To prevent the total longitudinal tire force and desired yaw moment from exceeding the constraints, a relaxation factor ε and its weighting coefficient ρ are introduced as

$$\begin{aligned} \min J &= Q_E ||B_E \tilde{u} - \Delta M_{z,\text{des}}||_2 + R_E ||C_E \tilde{u}||_2 + \rho \varepsilon^2 \\ &= \tilde{u}^T (Q_E B_E^T B_E + R_E C_E^T C_E) \tilde{u} + \rho \varepsilon^2 \\ &\quad - 2Q_E \Delta M_{z,\text{des}} B_E \tilde{u} + \underbrace{Q_E \Delta M_{z,\text{des}}^2}_{\text{Constant}} \end{aligned} \quad (40)$$

where $\tilde{u} = [T_{fl}, T_{fr}, T_{rl}, T_{rr}]^T$, $B_E = \frac{1}{R_w} [-l_w \cos \delta_f + l_f \sin \delta_f, l_w \cos \delta_f + l_f \sin \delta_f, -l_w, l_w]^T$ and $C_E = \frac{1}{(\mu R_w)^2} \text{diag}(F_{zfl}^{-2}, F_{zfr}^{-2}, F_{zrl}^{-2}, F_{zrr}^{-2})$.

The constraints of actuators are given by

$$\begin{cases} T_{\text{des}} = [1 \ 1 \ 1 \ 1] \cdot \tilde{u} + \varepsilon, \\ \Delta T_{ij}^{\min} \leq \Delta T_{ij} \leq \Delta T_{ij}^{\max}, \\ T_{ij} \geq \max \left(R_w \sqrt{(\mu F_{zij})^2 - (F_{yij})^2}, T_{ij}^{\min} \right) \\ T_{ij} \leq \min \left(R_w \sqrt{(\mu F_{zij})^2 - (F_{yij})^2}, T_{ij}^{\max} \right) \\ 0 \leq \varepsilon \leq \varepsilon_{\max} \end{cases} \quad (41)$$

where T_{ij}^{\min} and T_{ij}^{\max} represent the minimum and maximum values of wheel torque; ΔT_{ij}^{\min} and ΔT_{ij}^{\max} are the minimum and maximum values of wheel torque increment; ε is the maximum relaxation factor.

Equation (41) can be reformulated in the quadratic form as

$$\min J = \frac{1}{2} \mathbf{u}_E^T \mathbf{H}_E \mathbf{u}_E + \mathbf{f}_E^T \mathbf{u}_E \quad (42)$$

where

$$\begin{aligned} \mathbf{H}_E &= \begin{bmatrix} \mathbf{Q}_E \mathbf{B}_E^T \mathbf{B}_E + \mathbf{R}_E \mathbf{C}_E^T \mathbf{C}_E & 0_{4 \times 1} \\ 0_{1 \times 4} & \rho \end{bmatrix}, \\ \mathbf{f}_E &= \begin{bmatrix} -\mathbf{B}_E^T \Delta M_{z,\text{des}}^T \mathbf{Q}_E^T & 0 \end{bmatrix}, \quad \mathbf{u}_E = [\tilde{\mathbf{u}}^T \ \epsilon]^T \end{aligned}$$

An event-triggered slip ratio controller is proposed to ensure precise execution of the wheel torque while ensuring a low wheel slip ratio. If the wheel slip ratio exceeds the triggered threshold and is maintained for more than 5 ms, the SMC controller will be activated; if the slip ratio is below the triggered threshold and is maintained for more than 10 ms, the SMC controller will be deactivated. The sliding mode surface and reaching law of the wheel slip ratio controller are given by

$$s_{ij} = \omega_{ij} - \omega_{\text{ref}} \quad (43)$$

$$\dot{s}_{ij} = -\varepsilon_E \text{sat}(s_{ij}) \quad (44)$$

where ω_{ref} is the reference wheel rational speed and ε_E is the coefficient of the constant-speed convergence term.

Combining with Eq. (37), the torque for maintaining the desirable slip ratio can be derived as

$$T_{wij} = I_w (\dot{\omega}_{ij,\text{ref}} - \varepsilon_E \text{sat}(s_{ij})) + F_{xij} R_w \quad (45)$$

where $\dot{\omega}_{ij,\text{ref}}$ is calculated based on Eq. (5) when $\kappa_{ij} = 0.1 \text{sign} T_{ij}$.

Finally, the wheel torque is derived as

$$T_{wij} = \begin{cases} T_{ij}, & |\kappa_{ij}| \leq 0.1 \\ I_w (\dot{\omega}_{ij,\text{ref}} - \varepsilon_E \text{sat}(s_{ij})) + F_{xij} R_w, & |\kappa_{ij}| > 0.1 \end{cases} \quad (46)$$

Theorem 1: For the system described by Eq. (26), if the reaching law Eq. (27) are chosen under the control variable Eq. (28), the control system can achieve global asymptotic stability.

5 Stability Analysis of the Proposed Control Scheme

To guarantee the reliability of the proposed control scheme, a stability analysis of the longitudinal and lateral controllers is imperative.

5.1 Longitudinal Controller

For longitudinal control, a sliding mode controller is employed to realize longitudinal vehicle speed tracking. The stability of SMC can be validated using the Lyapunov method. The Lyapunov function is constructed as

$$V = \frac{1}{2} s^T s \quad (47)$$

where s is the sliding mode surface.

The derivative of Eq. (47) is then calculated by

$$\dot{V}(x, t) = s \cdot \dot{s} \leq 0 \quad (48)$$

where \dot{s} is the reaching law.

According to the SMC's exponential reaching law, the signs of s and \dot{s} are opposite. That is to say, when $\dot{s} < 0$, $s > 0$; when $\dot{s} > 0$, $s < 0$ and when $\dot{s} = 0$, $s = 0$. Therefore, $\dot{V} \leq 0$ is guaranteed so as to ensure the Lyapunov stability. Similarly, the design law of the yaw stability & yaw angle compensation controller Eq. (28) and the wheel slip ratio controller Eq. (45) also satisfy the Lyapunov stability criterion.

5.2 Lateral Controller

An MPC and a SMC controller are developed to realize lateral trajectory tracking. The abstract architecture of the proposed trajectory tracking and stability control system is shown in Fig. 10.

The impacts of MPC on SMC are first analyzed. MPC trajectory tracking control mainly affects the reference yaw rate through the front-wheel steering angle, which in turn affects the SMC's output additional yaw moment. Therefore, it is only to prove the stability of SMC to ensure the stability of the lateral stability and yaw angle compensation system. For the SMC stability analysis, the readers can refer to Subsect. 5.1 for details.

This paper focuses on analyzing the impact of SMC-based additional yaw moment on the MPC-based front-wheel steering control. By taking an additional yaw moment as a system disturbance as shown in Eq. (13), the system can be transformed into

$$\begin{cases} \mathbf{x}_{k+1} = \mathbf{A}_k \mathbf{x}_k + \mathbf{B}_k \mathbf{u}_k + \boldsymbol{\Phi}_k \mathbf{w}_k \\ \mathbf{y}_k = \mathbf{C}_k \mathbf{x}_k \end{cases} \quad (49)$$

where $\mathbf{w}_k = [\Delta F_{x,\text{des}}, 0, 0, \Delta M_{z,\text{des}}, 0, 0]$; $\boldsymbol{\Phi}_k$ can be expressed by

$$\Phi_k = \begin{bmatrix} 1 & 0 & 0 & 0 & 0 & 0 \\ 0 & 0 & 0 & 0 & 0 & 0 \\ 0 & 0 & 0 & 0 & 0 & 0 \\ 0 & 0 & 0 & 1 & 0 & 0 \\ 0 & 0 & 0 & 0 & 0 & 0 \\ 0 & 0 & 0 & 0 & 0 & 0 \end{bmatrix} \quad (50)$$

The system disturbance $\Delta F_{x,\text{des}}$ and $\Delta M_{z,\text{des}}$ are bounded, which are determined by actuators and road friction. The system stability analysis can be transformed into the disturbance bounded MPC stability problem. It is worth noting that MPC exhibits a certain degree of robustness. This is because the state x_{k+1} is jointly determined by x_k and u_k , while the input u_k is optimized through the current state feedback x_k and the reference state. The current state feedback x_k is the result of the joint action of external disturbances w_k . Thus, the control variable u_k has a certain degree of robustness. The stability analysis of MPC is given as follows:

According to Eq. (19), the objective function can be expressed as

$$J_k = \sum_{i=1}^N \ell(\hat{x}_{k+i|k}, \hat{u}_{k+i-1|k}) \quad (51)$$

where $\ell(x, u) \geq 0$, if and only if $x=0$ and $u=0$, $\ell(x, u)=0$. At the same time, the terminal constraints should satisfy

$$\hat{x}_{k+N|k} = 0 \quad (52)$$

and x and u satisfy

$$\hat{x}_{k+i|k} \in X, \hat{u}_{k+i|k} \in U \quad (53)$$

This paper utilizes a Lyapunov function to demonstrate the stability of MPC. The goal is to identify a Lyapunov function for the system that is positive definite and has a negative definite derivative. The chosen Lyapunov function is the cost function as shown in Eq. (19). Its positive definiteness has been clarified in the previous assumptions (see Eq. (51) to (53)). Hence, the focus is on proving the negative definiteness of its derivative. The analysis process is outlined as follows.

$$\begin{aligned} J_{k+1}^0 &= \min_u \sum_{i=1}^N \ell(x_{k+i+1}, u_{k+i}) \\ &= \min_u \left\{ \sum_{i=1}^N \ell(x_{k+i}, u_{k+i-1}) - \ell(x_{k+1}, u_k) \right. \\ &\quad \left. + \ell(x_{k+1+N}, u_{k+N}) \right\} \\ &= -\ell(x_{k+1}, u_k) + \min_u \left\{ \sum_{i=1}^N \ell(x_{k+i}, u_{k+i-1}) \right. \\ &\quad \left. + \ell(x_{k+1+N}, u_{k+N}) \right\} \\ &\leq -\ell(x_{k+1}, u_k^0) + J_k^0 + \min_u \{\ell(x_{k+1+N}, u_{k+N})\} \end{aligned} \quad (54)$$

According to the terminal constraints (52), we can get

$$\min_u \{\ell(x_{k+1+N}, u_{k+N})\} = 0 \quad (55)$$

and $\ell(x_{k+1}, u_k^0) \geq 0$, thus $J_{k+1}^0 \leq J_k^0$.

6 Experimental Validation and Discussions

In order to demonstrate the effectiveness of the proposed control scheme, comparative tests were performed on a specialized hardware-in-the-loop (HIL) test platform, as depicted in Fig. 11. The HIL platform comprises an ETAS LabCar realtime simulator, two master computers, and a Vector CAN bus device (CANoe).

Master Computer-1 aims to configure the high-fidelity vehicle model, sensor model, and test procedure in CarSim. In the Master Computer-1, the steering wheel angle and the four-wheel drive torque of the Carsim vehicle model are set as import channels, and the measurable information from the sensors, such as the vehicle inertial states and positions, are set as export channels. The configured CarSim vehicle model is then integrated into the ETAS Labcar development environment, where the CarSim import and export channels are assigned to the predefined CAN protocol. The ETAS Labcar project can be compiled and loaded into ETAS LabCar realtime simulator as a controlled object. The specifications of the test vehicle is presented in Table 1.

Master Computer-2 is used to develop the proposed control scheme in Matlab Simulink and also serves as an onboard domain controller to run the developed control scheme in real-time by using CANoe HIL mode. Additionally, CANoe is also used to record the test results. The ETAS LabCar simulator operates by running the CarSim vehicle model in real-time and transmitting vehicle sensor signals to the CAN bus. It also receives control commands from the Master Computer-2. The control period of the proposed control scheme is set as 10 ms, which is consistent with the widely used CAN bus communication cycle. CarSim vehicle

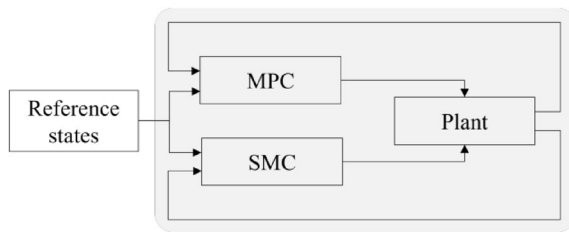


Fig. 10 The abstract architecture of the proposed trajectory tracking and stability control system



Fig. 11 HIL testing platform

Table 1 The specifications of the test vehicle and the key parameters of the controller

Symbol	Description	Values
m	Vehicle mass	1270 kg
I_{zz}	Vehicle moment of inertia	1536.7 kg·m ²
l_f	Distance from front axle to mass center	1.015 m
l_r	Distance from rear axle to mass center	1.895 m
l_w	Track width	1.675 m
R_w	Wheel radius	0.325 m
N_p	Prediction horizon	10
N_c	Control horizon	5
T_p	MPC prediction time step	0.01
Q_A	Weight matrix of output	diag (100,1)
R_A	Weight coefficient of control	1
Q_E	Weight of additional yaw moment	1
R_E	Weight of tire using ratio	100
ρ	Weight coefficient of relaxation factor	1000

model, serving as the controlled object, runs in real-time in ETAS RTPC. To ensure simulation accuracy and calculation convergence, the update cycle of controlled object should be less than or equal to the control period. Thus, the update period of the CarSim vehicle model is set as 1 ms. The specifications of the HIL platform are presented in Table 2.

The double-lane change maneuver was used to simulate emergency obstacle avoidance, and its detailed formulations are provided as

$$Y_{\text{ref}}(X) = \frac{d_{y1}}{2}(1 + \tanh z_1) - \frac{d_{y2}}{2}(1 + \tanh z_2)$$

$$\psi_{\text{ref}}(X) = \arctan \left(d_{y1} \left(\frac{1}{\cosh z_1} \right)^2 \left(\frac{1.2}{d_{x1}} \right) - d_{y2} \left(\frac{1}{\cosh z_2} \right)^2 \left(\frac{1.2}{d_{x2}} \right) \right) \quad (56)$$

$$\text{where } z_1 = \frac{2.4}{d_{x1}}(X - 27.19) - 1.2, \quad z_2 = \frac{2.4}{d_{x2}}(X - 56.46) - 1.2,$$

$$d_{x1} = 25, \quad d_{x2} = 21.95, \quad d_{y1} = 4.05, \quad d_{y2} = 5.7.$$

The reference yaw angle needs to take into account the impact of the sideslip angle, where $\varphi_{\text{ref}} = \psi_{\text{ref}} - \beta$ is given.

To demonstrate the control performance of the proposed control strategy, three different trajectory tracking strategies are selected as benchmarks to highlight the superiority of the proposed control scheme. Controller A represents the integrated lateral-longitudinal trajectory tracking controller (MPC and SMC), Controller B denotes the control scheme enhanced with yaw angle compensation control, Controller C is the proposed trajectory tracking scheme with improved vehicle yaw stability based on Controller A. Controller D represents the state-of-the-art trajectory tracking by yaw moment control [22]. In Controller D, an integrated MPC is established to track the lateral deviation, heading angle deviation, sideslip angle, and yaw rate to obtain the optimal solution for the front-wheel angle and additional yaw moment, ensuring the handling stability and trajectory tracking accuracy.

6.1 Scenario 1: Reference $v_x = 70 \text{ km/h}$, $\mu = 0.8$

All four controllers exhibit excellent trajectory tracking performance in Scenario 1 as depicted in Fig. 12. However, the sideslip angles and yaw rates are smaller for Controllers C and D. The stability control algorithm in Controller C was briefly triggered to suppress the vehicle's yaw rate while reducing lateral displacement, resulting in improved vehicle dynamics stability. All the controllers exhibit comparable tracking accuracies, but Controller A displays significant fluctuations in yaw rate and has a higher peak sideslip angle, which may potentially compromise ride comfort. Controller B enhances vehicle maneuverability while effectively reducing the yaw angle tracking errors and sideslip angles. Controllers C and D exhibit identical effects on lateral stability control. A careful examination of Fig. 12(f) reveals that

Table 2 The specifications of the HIL platform

Name	Type
Master computer-1	intel(R) Core(TM) i7-2600 CPU @ 3.40 GHz, 8G RAM
Master computer-2	intel(R) Core(TM) i7-12700H CPU @ 2.70 GHz, 16G RAM
ETAS LabCar real-time simulator	intel(R) Core(TM) i7-3770 CPU @ 3.44 GHz, 2×4 GB DDR2-SD RAM
CAN hardware	Vector 1640A, CANoe 12.0 SP4

Controller C demonstrates a smaller value for the side slip angle, indicating a higher level of stability. All the controllers use the same longitudinal velocity tracking controller and torque distribution module. Controller A demonstrates poor performance due to the significant disturbances caused by rapid changes in yaw angle and yaw rate, and notable errors resulting from linearization assumptions.

6.2 Scenario 1: Reference $v_x = 90 \text{ km/h}$, $\mu = 0.8$

The maximum yaw rate of the reference trajectory exceeds the limit the road can provide. If the vehicle is expected to track the desired trajectory with small errors, the sideslip angle would vary over a wide range. Thus, sacrificing the

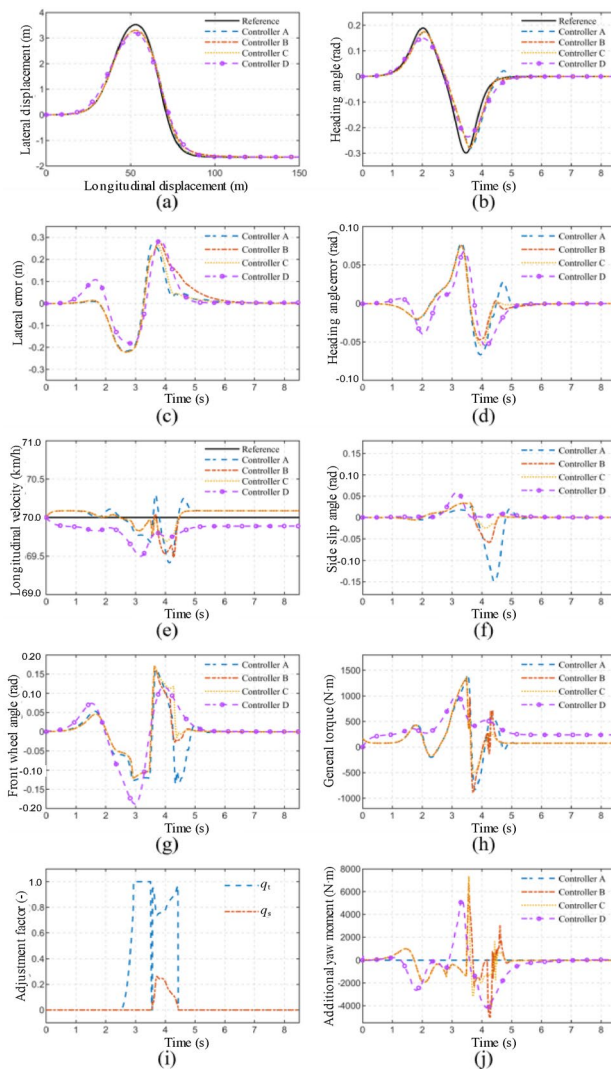


Fig. 12 The testing results under Scenario 1. **a** is the trajectory, **b** is the heading angle, **c** is the lateral trajectory tracking error, **d** is the heading angle error, **e** is the longitudinal velocity, **f** is the vehicle side slip angle, **g** is the front wheel steering angle, **h** is the general torque, **i** is the adjustment factor, and **j** is the additional yaw moment

tracking accuracy to a certain extent is necessary to ensure vehicle dynamics stability. From Fig. 13, Controller A exhibits a comparable tracking accuracy to Controllers B, C and D, but the maximum sideslip angle reaches -0.43 rad , requiring the intervention of the yaw stability control to enhance vehicle dynamics stability. In the meantime, Controllers B and C can effectively reduce both yaw angle tracking errors and sideslip angles. Controller B performs better in suppressing the sideslip angle, with a variation range of only $\pm 0.08 \text{ rad}$. However, it shows relatively poor performance in tracking the yaw angle, with an obvious chattering phenomenon during convergence. Seen from Fig. 13(f), the maximum side slip angle of Controller D reaches 0.36 rad . This is due to that the control system necessitates the simultaneous output of the front-wheel steering angle and an additional yaw moment, making it difficult to achieve coordinated trajectory tracking and stability control through dynamically adjusting the weight coefficients under high-speed conditions.

Controller A remains unstable for an extended period, while Controller B and C significantly reduce the time of instability. As mentioned in Ref. [31], the early intervention of the stability control system helps improve the stability control performance. According to the modified vehicle yaw stability criterion in this study, the stability control of Controller C can be activated before reaching the boundaries, when the state tends to approach the boundaries. It can effectively enhance the vehicle stability and increases the tire utilization ratios.

6.3 Scenario 1: Reference $v_x = 100 \text{ to } 70 \text{ km/h}$, $\mu = 1 \text{ to } 0.6$

In Scenario 3, the initial vehicle velocity is set at 100 km/h , and it decelerates to 70 km/h with a constant deceleration. The road friction coefficient undergoes a sudden change from 1.0 to 0.6 at the position of 60 m . This scenario is designed to simulate the vehicle performing a deceleration and lane change maneuver while experiencing a sudden decrease in tire-road adhesion. For clarity, a diagram is provided to illustrate the testing conditions in details, as shown in Fig. 14.

The test results are presented in Figs. 15 and 16. From Fig. 15(a)–(d), it is evident that the proposed control scheme demonstrates superior control performance compared to the other three controllers. During the interval between 1.01 s and 1.72 s , despite the vehicle's instability as illustrated in Fig. 16(a), compensating for the tracking error remains a primary concern. Upon reaching a low-adhesion road (after 2.4 s), the test vehicle is susceptible to lateral instability. In this phase, the objectives and outputs of the SMC controller are dynamically adjusted by the weighting coefficients q_t and q_s as illustrated in Fig. 15(i). This indicates that the proposed

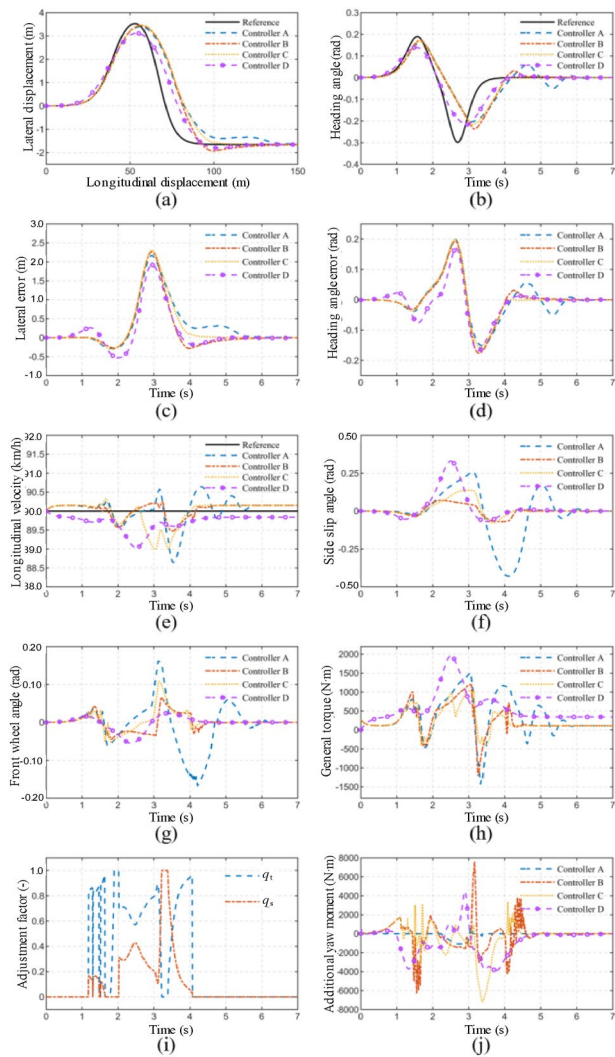


Fig. 13 The testing results under Scenario 2. **a** is the trajectory, **b** is the heading angle, **c** is the lateral trajectory tracking error, **d** is the heading angle error, **e** is the longitudinal velocity, **f** is the vehicle side slip angle, **g** is the front wheel steering angle, **h** is the general torque, **i** is the adjustment factor, and **j** is the additional yaw moment

control scheme can generate an additional yaw moment, which can be used to regulate the vehicle's yaw motion and while suppressing the vehicle sideslip angle. As observed in Fig. 15(j), the additional yaw moment generated by Controller C is smaller than that of Controller B, exhibiting a smoother control process. As demonstrated in Fig. 16(c)–(f), Controller A exhibits the highest tire utilization due to the absence of stability control, while Controller C exhibits the lowest tire adhesion utilization. This means the proposed control scheme has a considerable reservation space for tire force allocation, indicating higher vehicle stability.

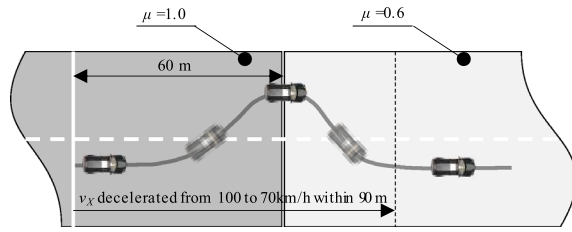


Fig. 14 The diagram of Scenario 3

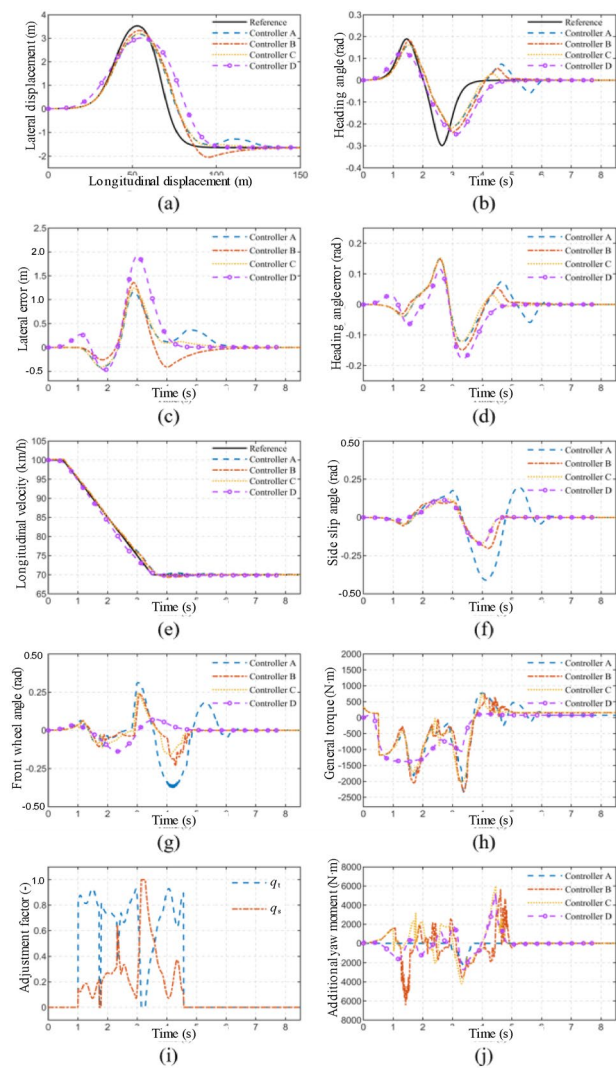


Fig. 15 The testing results under Scenario 3. **a** is the trajectory, **b** is the heading angle, **c** is the lateral trajectory tracking error, **d** is the heading angle error, **e** is the longitudinal velocity, **f** is the vehicle side slip angle, **g** is the front wheel steering angle, **h** is the general torque, **i** is the adjustment factor, and **j** is the additional yaw moment

6.4 Comprehensive Comparison and Discussions

The performances of all the controllers are compared based on several aspects: lateral trajectory, yaw angle, longitudinal

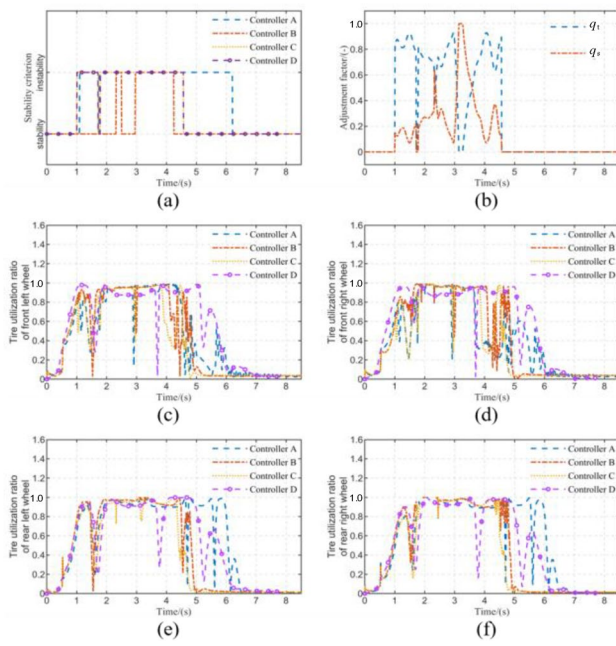


Fig. 16 The testing results under Scenario 3. **a** is the vehicle stability state, **b** is the adjustment factor, **c** is the tire utilization of front left wheel, **d** is the tire utilization of front right wheel, **e** is the tire utilization of rear left wheel, and **f** is the tire utilization of rear right wheel

velocity, vehicle sideslip angle, yaw rate, front wheel steering angle, tire utilization, and unstable time. Taking Controller A as the baseline, the performance indicators regarding the mentioned aspects are calculated by

$$\text{Performance index} = \frac{\text{RMS}_A - \text{RMS}_{B/C/D}}{\text{RMS}_A}$$

where RMS is the Root-Mean-Squared Error.

According to Fig. 17, the unstable time of the four controllers is comparable, but Controller C and D exhibit significant improvements in yaw angle error, sideslip angle, yaw rate, and front-wheel angle compared to Controller A and B. Both Controller C and D can ensure trajectory tracking accuracy while enhancing vehicle stability. Additionally, the proposed control method exhibits superior performance than controller D in terms of longitudinal speed and tire utilization ratio.

The proposed control scheme mainly includes two parts: trajectory tracking and stability control. The sliding mode control method used in stability control is a low computational cost method that has been widely applied in industrial products. The main computational cost of the proposed method comes from the MPC optimization. The MPC algorithm is currently used in most intelligent driving products. In this paper, CANoe HIL mode is used to set the laptop as a real-time controller. The CPU of the laptop is 2.5 GHz, and

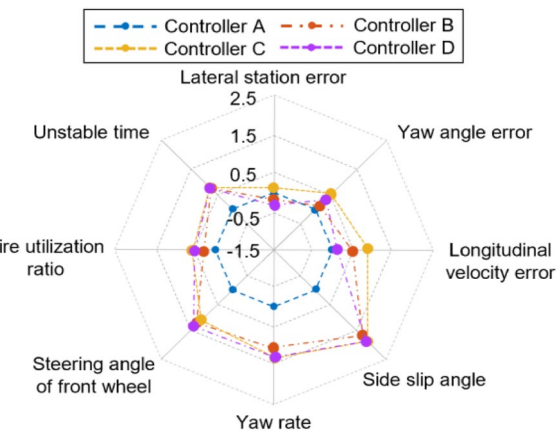


Fig. 17 Comprehensive comparison of the controllers' performance

its computing power is much lower than that of the mainstream intelligent driving computing centers. Therefore, the proposed control scheme can be implemented in real-time in practical application scenarios.

7 Conclusions

This paper presents a cooperative trajectory tracking and stability control scheme for FWID EVs to simultaneously improve trajectory tracking accuracy and vehicle yaw stability. First, a modified phase plane method is developed for vehicle yaw stability assessment by analyzing the three-dimensional phase trajectory. Then, an MPC controller with a variable stiffness tire model is presented to improve lateral trajectory tracking accuracy. A dual-weight cooperative sliding mode control method is further established for yaw angle tracking compensation and yaw stability control. The desirable additional yaw moment and total longitudinal tire force are realized through optimal torque allocation while accounting for the slip ratio of each tire. Finally, the performance of the proposed control scheme is verified under high-speed double-lane change maneuvers. For future real-world applications, the accurate estimation of tire road adhesion and real-time estimation of key vehicle state parameters represent the main challenges and potential avenues for modifications.

Acknowledgements This work is partly supported by the Taishan Scholars Program under Grant No.tsqn202312310 and partly supported by the China Postdoctoral Science Foundation under Grant No.2023M740244.

Declarations

Conflict of interest The corresponding author declares that there is no conflict of interest between all the authors.

References

1. Cai, W., Wu, X., Zhou, M., Liang, Y., Wang, Y.: Review and development of electric motor systems and electric powertrains for new energy vehicles. *Automot. Innov.* **4**, 3–22 (2021)
2. Sun, F.: Green energy and intelligent transportation-promoting green and intelligent mobility. *Green Energy Intell. Transp.* **1**(1), 100017 (2022)
3. Zhang, H., Liu, C., Zhao, W.: Segmented trajectory planning strategy for active collision avoidance system. *Green Energy Intell. Transp.* **1**(1), 100002 (2022)
4. Xu, S., Liu, Q., Hu, Y., Xu, M., Hao, J.: Decision-making models on perceptual uncertainty with distributional reinforcement learning. *Green Energy Intell. Transp.* **2**(2), 100062 (2023)
5. Chen, Y., Chen, S., Ren, H., Gao, Z., Liu, Z.: Path tracking and handling stability control strategy with collision avoidance for the autonomous vehicle under extreme conditions. *IEEE Trans. Veh. Technol.* **69**(12), 14602–14617 (2020)
6. Guo, N., Zhang, X., Zou, Y.: Real-time predictive control of path following to stabilize autonomous electric vehicles under extreme drive conditions. *Automot. Innov.* **5**(4), 453–470 (2022)
7. Li, J., Cheng, H., Guo, H., Qiu, S.: Survey on artificial intelligence for vehicles. *Automot. Innov.* **1**, 2–14 (2018)
8. Brown, M., Gerdes, J.C.: Coordinating tire forces to avoid obstacles using nonlinear model predictive control. *IEEE Trans. Intell. Veh.* **5**(1), 21–31 (2019)
9. Xu, L., Wang, Y., Sun, H., Xin, J., Zheng, N.: Integrated longitudinal and lateral control for Kuafu-II autonomous vehicle. *IEEE Trans. Intell. Transp. Syst.* **17**(7), 2032–2041 (2015)
10. Tong, Y., Li, C., Wang, G., Jing, H.: Integrated path-following and fault-tolerant control for four-wheel independent-driving electric vehicles. *Automot. Innov.* **5**(3), 311–323 (2022)
11. Mirzaeinnejad, H., Mirzaei, M., Rafatnia, S.: A novel technique for optimal integration of active steering and differential braking with estimation to improve vehicle directional stability. *ISA Trans.* **80**, 513–527 (2018)
12. Farag, W.: Complex trajectory tracking using PID control for autonomous driving. *Int. J. Intelligent Transp. Syst. Res.* **18**(2), 356–366 (2020)
13. Wang, X., Wang, D., Du, M., Song, K., Ni, Y., Li, Y.: A two-layer trajectory tracking control scheme of manipulator based on ELM-SMC for autonomous robotic vehicle. *IEEE Trans. Autom. Sci. Eng.* **21**(3), 2337–2348 (2024)
14. Park, M., Kang, Y.: Experimental verification of a drift controller for autonomous vehicle tracking: a circular trajectory using LQR method. *Int. J. Control. Autom. Syst.* **19**(1), 404–416 (2021)
15. Naranjo, J.E., Sotelo, M.A., Gonzalez, C., Garcia, R., De Pedro, T.: Using fuzzy logic in automated vehicle control. *IEEE Intell. Syst.* **22**(1), 36–45 (2007)
16. Liang, Y., Li, Y., Yu, Y., Zhang, Z., Zheng, L., Ren, Y.: Path-following control of autonomous vehicles considering coupling effects and multi-source system uncertainties. *Automot. Innov.* **4**, 284–300 (2021)
17. Xue, W., Zheng, L.: Active collision avoidance system design based on model predictive control with varying sampling time. *Automot. Innov.* **3**(1), 62–72 (2020)
18. Spielberg, N.A., Brown, M., Gerdes, J.C.: Neural network model predictive motion control applied to automated driving with unknown friction. *IEEE Trans. Control Syst. Technol.* **30**(5), 1934–1945 (2021)
19. Chen, L., Zou, K., Cai, Y., Teng, C., Sun, X., Wang, H.: Longitudinal and lateral comprehensive trajectory tracking control of intelligent vehicles based on NMPC. *Automot. Eng.* **43**(2), 153–161 (2021)
20. Lin, F., Zhang, Y., Zhao, Y., Yin, G., Zhang, H., Wang, K.: Trajectory tracking of autonomous vehicle with the fusion of DYC and longitudinal-lateral control. *Chin. J. Mech. Eng.* **32**, 1–16 (2019)
21. Xu, X., Lu, S., Chen, L., Cai, Y., Li, Y.: Trajectory tracking of distributed-drive self-driving vehicle based on coordination between autonomous steering and differential steering. *Automot. Eng.* **40**(4), 475–481 (2018)
22. Zhai, L., Wang, C., Hou, Y., Liu, C.: MPC-based integrated control of trajectory tracking and handling stability for intelligent driving vehicle driven by four hub motor. *IEEE Trans. Veh. Technol.* **71**(3), 2668–2680 (2022)
23. Zhang, S., Zhao, X., Zhu, G., Shi, P., Hao, Y., Kong, L.: Adaptive trajectory tracking control strategy of intelligent vehicle. *Int. J. Distrib. Sens. Netw.* **16**(5), 1550147720916988 (2020)
24. Hu, C., Wang, R., Yan, F.: Integral sliding mode-based composite nonlinear feedback control for path following of four-wheel independently actuated autonomous vehicles. *IEEE Trans. Transp. Electrif.* **2**(2), 221–230 (2016)
25. Cheng, S., Li, L., Guo, H.-Q., Chen, Z.-G., Song, P.: Longitudinal collision avoidance and lateral stability adaptive control system based on MPC of autonomous vehicles. *IEEE Trans. Intell. Transp. Syst.* **21**(6), 2376–2385 (2020)
26. Zhang, Z., Zheng, L., Li, Y., Li, S., Liang, Y.: Cooperative strategy of trajectory tracking and stability control for 4wid autonomous vehicles under extreme conditions. *IEEE Trans. Veh. Technol.* **72**(3), 3105–3118 (2023)
27. Hang, P., Xia, X., Chen, G., Chen, X.: Active safety control of automated electric vehicles at driving limits: a tube-based MPC approach. *IEEE Trans. Transp. Electrif.* **8**(1), 1338–1349 (2022)
28. Hajiloo, R., Abroshan, M., Khajepour, A., Kasaiezadeh, A., Chen, S.-K.: Integrated steering and differential braking for emergency collision avoidance in autonomous vehicles. *IEEE Trans. Intell. Transp. Syst.* **22**(5), 3167–3178 (2021)
29. Liang, Z., Zhao, J., Liu, B., Wang, Y., Ding, Z.: Velocity-based path following control for autonomous vehicles to avoid exceeding road friction limits using sliding mode method. *IEEE Trans. Intell. Transp. Syst.* **23**(3), 1947–1958 (2022)
30. Xie, J., Xu, X., Wang, F., Tang, Z., Chen, L.: Coordinated control based path following of distributed drive autonomous electric vehicles with yaw-moment control. *Control Eng. Pract.* **106**, 104–659 (2021)
31. Chen, W., Liu, X., Huang, H., Yu, H.: Research on side slip angle dynamic boundary control for vehicle stability control considering the impact of road surface. *J. Mech. Eng.* **48**(14), 112–118 (2012)
32. Slotine, J.E., Li, W.: *Applied Nonlinear Control*. Englewood Cliffs, New Jersey (1991)
33. Sadri, S., Wu, C.: Stability analysis of a nonlinear vehicle model in plane motion using the concept of Lyapunov exponents. *Veh. Syst. Dyn.* **51**(6), 906–924 (2013)
34. Meng, F., Shi, S., Zhang, B., Bai, M., Lin, N.: Analysis for global characteristics of Lyapunov exponents in vehicle plane motion system. *Sci. Rep.* **12**(1), 9300 (2022)
35. Ono, E., Hosoe, S., Tuan, H.D., Doi, S.I.: Bifurcation in vehicle dynamics and robust front wheel steering control. *IEEE Trans. Control Syst. Technol.* **6**(3), 412–420 (1998)
36. Bobier-Tiu, C.G., Beal, C.E., Kegelman, J.C., Hindiyeh, R.Y., Gerdes, J.C.: Vehicle control synthesis using phase portraits of planar dynamics. *Veh. Syst. Dyn.* **57**(9), 1318–1337 (2018)
37. Xiong, L., Qu, T., Feng, Y., Deng, L.: Stability criterion for the vehicle under critical driving situation. *J. Mech. Eng.* **51**(10), 103–111 (2015)
38. Huang, Y., Liang, W., Chen, Y.: Stability regions of vehicle lateral dynamics: Estimation and analysis. *J. Dyn. Syst. Meas. Contr.* **143**(5), 051002 (2021)

39. Subosits, J.K., Gerdes, J.C.: Impacts of model fidelity on trajectory optimization for autonomous vehicles in extreme maneuvers. *IEEE Trans. Intell. Veh.* **6**(3), 546–558 (2021)
40. Pacejka, H.B., Bakker, E.: The magic formula tyre model. *Veh. Syst. Dyn.* **21**(S1), 1–18 (1992)
41. Beal, C.E., Boyd, C.: Coupled lateral-longitudinal vehicle dynamics and control design with three-dimensional state portraits. *Veh. Syst. Dyn.* **57**(2), 286–313 (2019)

Springer Nature or its licensor (e.g. a society or other partner) holds exclusive rights to this article under a publishing agreement with the author(s) or other rightsholder(s); author self-archiving of the accepted manuscript version of this article is solely governed by the terms of such publishing agreement and applicable law.